Chinese Chemical Letters 34 (2023) 108187

Contents lists available at ScienceDirect

Chinese Chemical Letters

journal homepage: www.elsevier.com/locate/cclet

Lignin derived porous carbon with favorable mesoporous contributions for highly efficient ionic liquid-based supercapacitors

Jia Liu*, Xiu-Wen Mei, Feng Peng*

Beijing Key Laboratory of Lignocellulosic Chemistry, MOE Engineering Research Center of Forestry Biomass Materials and Bioenergy, Beijing Forestry University, Beijing 100083, China

ARTICLE INFO

Article history:
Received 21 November 2022
Revised 16 December 2022
Accepted 31 January 2023
Available online 3 February 2023

Keywords:
Lignin
Porous carbon
Favorable mesoporous contributions
Low heteroatom content
Supercapacitors

ABSTRACT

Lignin and its derivatives hold great potential in developing high performance porous carbon materials for supercapacitors due to the versatile features of high carbon content, abundant multifunctional groups, low cost, and environmental benefits. Unfortunately, their derived porous carbon generally has the features of unfavorable microporous-dominated morphologies and low specific surface area (SSA) attributed from the highly-branched structure of lignin, which are hardly suitable for the supercapacitors with ionic liquid (IL) electrolyte, leading to poor energy density and rate capability. Herein, porous carbon materials with desirable mesoporous contributions from sodium lignosulphonate are designed *via* a facile template method. Such rich mesoporisity carbon materials not only possess with three-dimensional interconnected network, large SSA, as well as favorable pore size distribution for accelerated ion and electron mass transfer, but also feature low heteroatom content for high electrochemical stability. Consequently, the optimal electrode exhibits a high capacitance of 166 F/g at 0.5 A/g, superior rate performance (59 Wh/kg at 59 kW/kg), as well as impressive cycle life with good capacitance retention of 93.1% in $EMIBF_4$ electrolytes. The present work opens a new avenue to design porous carbon materials with high mesopore properties from lignin for effective compatibility with IL electrolyte in high-performance supercapacitors.

The ever-flourishing electric vehicles, portable electronic devices and stationary energy storage systems have attracted worldwide attention towards high energy– power density electrochemical storage devices [1–5]. Supercapacitors hold the advantages of high-power output capability, fast charge-discharge rate, and long-time cycling stability, showing tremendous potential in high-power designs [6–9]. Unfortunately, their practical applications have long been constrained by the relatively poor energy density (5–20 Wh/kg) [10–12]. Theoretically, the energy density (E) of supercapacitors is determined by the operation voltage (V) and capacitance (C) according to the equation, $E = 0.5CV^2$ [13,14]. That is, a high E can be obtained by increasing C or enlarging V. In this regard, ionic liquid (IL) electrolyte with wide voltage window (3.7–5 V) exhibits a prominent superiority compared to its aqueous electrolyte counterparts (about 1 V) [15–17]. Besides, the peculiarities of low volatility and non-flammability also render IL effectively avoid the safety hazards caused by leakage and flame of conventional organic electrolyte [18–20]. Nevertheless, their intrinsic high viscosity and large ionic size always lead to poor affinity to most carbon electrode materials with insufficient micropores structure (< 2 nm), thus resulting in sluggish ion diffusion kinetics and poor rate performance.

The porous carbon materials dominant with mesoporous active sites can provide plenty of ion-available diffusion channel for efficient mass transport, and therefore are strongly favored [21–28]. With that in mind, numerous advanced carbon electrode materials have been addressed and displayed excellent capacitance performance within IL electrolytes, including graphene, carbon nanofibers, carbon nanotube, carbon sphere, as well as active carbon with high mesoporous [29–34]. Nonetheless, most of them are produced from fossil fuels or unreproducible materials, which definitely detrimental to the sustainable development of resources and environment.

By virtue of the low-cost, renewability, and environmental benefits, many biomass materials have constantly been developed as potential precursors for porous carbon, such as carbohydrate, bagasse, lignin, and various primary biomasses [35–39]. Among them, lignin and its derivatives with high carbon content (more than 60 wt%), caused by their unique aromatic structure on natural macromolecule polymers, are considered as one of the most promising candidates [40–43]. In materials science, the high carbon content of biomass sources contributes to obtain bio-derived

* Corresponding authors.
E-mail addresses: liujia89@bjfu.edu.cn (J. Liu), fengpeng@bjfu.edu.cn (F. Peng).

https://doi.org/10.1016/j.cclet.2023.108187
1001-8417/

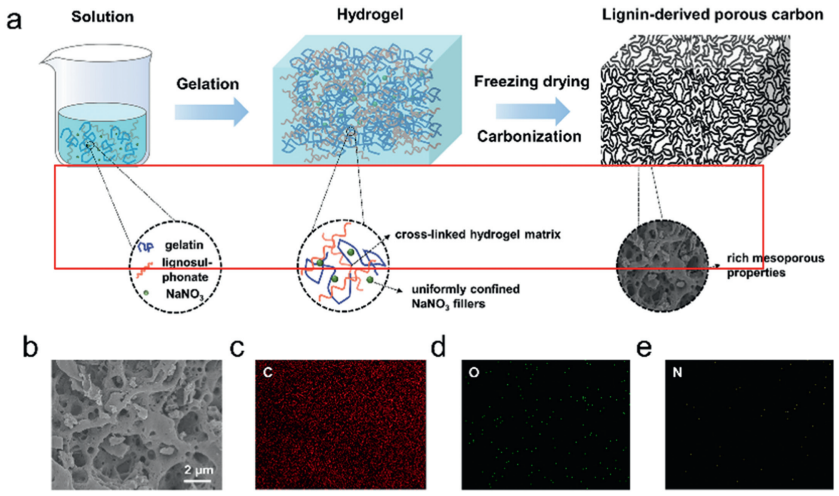

Fig. 1. (a) Schematic illustration for the synthesis of advanced lignin-derived porous carbons. (b) SEM image and corresponding EDS mappings of (c) C, (d) O and (e) N elements for LPC-0.5 sample.

carbon materials with high C/O ratios, giving rise to the improved conductive characteristics. Additionally, there are many functional groups (such as hydroxyl, methoxyl, carboxyl groups) on lignin, which not only help to introduce self-doped heteroatoms into carbon materials for good interface wettability, but also promote the formation of strong interchain entanglement and intermolecular bonds with environment [44–48]. Such interactions in turn offer emerging opportunities for effective preparation of porous carbon with controllable morphologies *via* advanced methods, such as template methods [49–51]. However, lignin is a complex and highly branched biopolymer consisting mainly of methoxylated phenylpropanoid acid units, such as *p*-hydroxyphenyl, guaiacol and butyl groups, cross-linked by various ether and carbon-carbon bonds. This highly branched structure leads to derived porous carbon generally featured with unfavorable pore distribution (microporous-dominated) and low specific surface area (SSA), which cannot match well with the ILs and severely degrades the rate capability at high current densities [52–54]. If the lignin-derived porous carbon can be built with controllable pore structure, the accelerated transfer kinetics and outstanding electrochemical performance can be therefore achieved.

In this contribution, we constructed a lignin-derived porous carbon with tunable mesostructure *via* a facile template strategy, in which sodium lignosulphonate worked as the major carbon sources, gelatin as binding agent, $NaNO_3$ as template and activator agent, respectively. In details, as shown in Fig. 1a, the sodium lignosulphonate, gelatin and $NaNO_3$ were firstly mixed in the water solution. Due to the water-soluble of sodium lignosulphonate and gelatin polymers, they can be easily dissolved into hot water to form a homogeneous sol on the molecular level. Subsequently, the sol was transformed into a physical cross-linked hydrogel matrix after cooling *via* interchain entanglement and intermolecular forces, attributing from the abundant multifunctional groups on these polymers. When freezing drying of hydrogel above, the $NaNO_3$ fillers could be simultaneously dispersed in aerogel scaffold as pore engineers for tuning porous structure. After carbonization, the advanced lignin-derived porous carbons were fabricated. Herein, the proper calcination temperature was identified to be 900 °C through preliminary experiments (Figs. S1–S3 in Supporting information). Finally, the as-obtained carbon materials, which denoted as LPC-X, X = 0.3, 0.4 and 0.5 (according to the weight ratio of $NaNO_3$ to total), were featured with not only 3D interconnected framework, high mesopore ratio and large SSA for fast ion adsorption/desorption and facilitated mass transfer, but also suitable heteroatoms doping for good interfacial wettability and high electrochemical stability. All these features collectively rendered the LPC electrode with superior specific capacitance, high energy-power density as well as excellent cycling lifespan.

The morphologies of as-prepared LPC-X (X = 0.3, 0.4 and 0.5) were examined by scanning electron microscope (SEM). As shown in Fig. 1b and Fig. S4 (Supporting information), all samples displayed typical 3D interconnected framework homogeneously decorated with numerous of pores. For detailed observations, elemental mapping images of LPC-0.5 were conducted, which illustrated that the C, O and small amounts of N elements were distributed uniformly on the 3D porous carbon scaffolds (Figs. 1c–e). Such a particular interconnected porous structure was beneficial to afford a continuous electron transfer pathway, short ion diffusion distance, and large contact area between electrode and electrolyte, thereby rendering the excellent electrochemical performance.

The detailed textural properties of as-synthesized carbon materials were further evaluated by N_2 adsorption-desorption measurements. As depicted in Fig. 2a, all LPC-Xs presented typical IV-type curves with steep adsorption regions at $P/P_0 < 0.1$ and distinctive H3-type hysteresis loops between $P/P_0 = 0.45$ and 0.9, indicative of the co-existence of micropores and mesopores [55,56]. Besides, the SSAs were also calculated as derived from Brunauer–Emmett–Teller theory, reaching to as large as 2176.6, 2407.6 and 2453.3 m^2/g for LPC-0.3, LPC-0.4 and LPC-0.5 samples, respectively (Table S1 in Supporting information). According to the pore size distributions displayed in Fig. 2b, all samples exhibited both micropores and mesopores structure, among which the micropore centered at 0.5–2 nm and the mesopore distributed around 2–5 nm, further confirming the hierarchical porous structures of LPC-Xs. Such small-size mesopore contributed to high availability of adsorption/desorption sites and shorten pathways of electrolyte ions, especially for IL electrolytes. Fig. 2c quantitatively described the contributions of mesopores to surface areas and pore volumes for all LPC-X samples, which denoted as S_{meso} and V_{meso}, respectively. It can be observed the mesopores could be tuned by increasing the dosage of $NaNO_3$, as the evidenced by the monotonic increased S_{meso} and V_{meso} from that of LPC-0.3 (738.4 m^2/g, 0.611 cm^3/g) to LPC-0.4 (1486.6 m^2/g, 1.284 cm^3/g), and then to LPC-0.5 (1955.5 m^2/g, 1.734 cm^3/g). Notably, all these values were much higher than that for the carbon material directly carbonization of lignin, successfully demonstrating the high mesopore properties of LPC-X samples (Fig. S5 in Supporting information). In addition, the rich mesoporisity was also reflected by the proportions

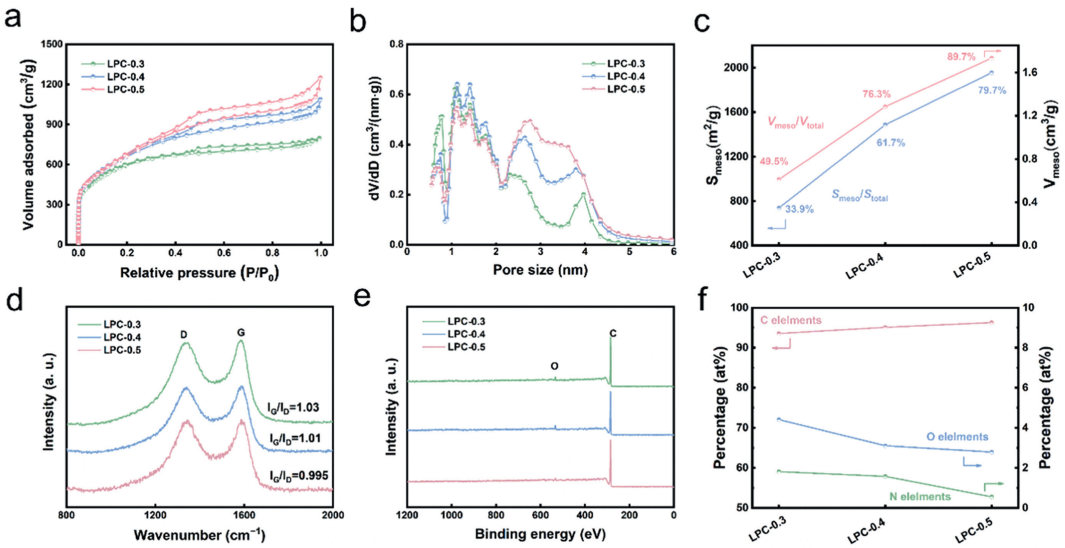

Fig. 2. The texture properties and surface chemistry of as-synthesized LPC-X (X = 0.3, 0.4 and 0.5) materials. (a) N_2 adsorption–desorption isotherms. (b) Pore size distribution curves. (c) The changes of S_{meso}, V_{meso}, S_{meso}/SSA and V_{meso}/V_{total} ratios for LPC-X samples. (d) Raman spectra. (e) XPS survey spectra. (f) The content variation of C, O and N elements for different materials.

of S_{meso} and V_{meso}, defined as S_{meso} /SSA and V_{meso} /V_{total}, shown in Fig. 2c, which indicated that the samples were all mesopore-dominated. Specifically, the S_{meso}/SSA and V_{meso}/V_{total} of LPC-0.5 sample reached the highest ratio of 79.7 and 89.7%, respectively. Overall, these mesopore-dominated hierarchical porous structures with favorable pore size and high SSA efficiently assured highly accessible sites for ion adsorption/desorption and facile kinetics for mass diffusion within IL electrolytes.

The Raman spectra of LPC-X (X = 0.3, 0.4 and 0.5) samples exhibited two typical broader peaks (Fig. 2d), corresponding to the well-documented G band (1580 cm^{-1}) and D band (1350 cm^{-1}), respectively. The intensity ratio of G band to D band (I_G/I_D) represented the graphitization degree of carbon materials. It can be observed that the I_G/I_D of LPC-0.3, LPC-0.4 and LPC-0.5 were 1.03, 1.01 and 0.995, respectively, indicating the relatively high texture ordering and graphitization degree of LPC-Xs. X-ray photoelectron spectroscopy (XPS) analyses were further conducted to investigate the surface chemistry of the obtained samples. The results in Fig. 2e clearly revealed the existence of C and O elements in all LPC samples. In addition, the contents of N elements for LPC-0.3, LPC-0.4 and LPC-0.5, respectively, were detected to be as low as 1.57, 1.89 and 0.55 at% (Table S2), and therefore made them difficult to be identified in the XPS survey spectra. The co-existence of C, O and N elements demonstrated in XPS results were well consistent with the EDS mapping observations aforementioned, further confirming the efficiency of $NaNO_3$-template synthesis strategy toward LPC in our work. Noteworthily, the concentrations of C elements were increased from 93.6 at% to 96.3 at%, while decreased for the O and N elements as the $NaNO_3$ increased (Fig. 2f). And the lowest O/N content of 2.96 at%/0.55 at% were detected on the LPC-0.5 samples. Actually, the presence of heteroatoms is regarded as a double-edged sword for the carbon electrode that paired with IL electrolytes [57]. On one hand, the doped heteroatoms could effectively improve the wettability between the electrode surface and electrolytes. On the other hand, excess heteroatoms would introduce unstable defects and functional groups on electrode materials, which can react with the electrolyte by undesired Faradaic processes, thus triggering the electrolyte decomposition and capacitance fade. Therefore, the relatively low content of O/N heteroatoms in LPC samples can effectively ensure the high electrochemical stability of IL electrolyte during cycling.

The electrochemical performances of LPC-X (X = 0.3, 0.4 and 0.5) were assessed in two-electrode coin-cell configurations with $EMIBF_4$ electrolyte. Fig. 3a displayed the cyclic voltammetry (CV) curves of the samples at 50 mV/s. Apparently, all the curves exhibited symmetrical rectangular shapes with very small distortion, revealing the ideal electric double layer behaviors. For comparison, the LPC-0.5 possessed the largest CV loop area as compared to other samples, indicative of the optimum capacitance properties arising from its high mesoporous structure, large SSA and favorable heteroatoms. Furthermore, the CV curves of LPC-0.5 were also measured at different scan rates, which illustrated the curves maintained the typical rectangular shapes even at 200 mV/s, successfully implying the high reversibility and excellent rate capability properties (Fig. 3b). The same phenomena were observed for other samples (Figs. S6 and S7 in Supporting information). Galvanostatic discharge-charge (GCD) curves of LPC-0.5 were recorded from 0.5 A/g to 50 A/g to further elucidate the high electrochemical performance (Figs. 3c and d). All curves displayed nearly linear and symmetrical triangle-like shapes with small IR drop, verifying the ideal capacitance performance of LPC-0.5. The specific capacitances of LPC-Xs calculated based on the GCD curves were plotted in Fig. 3e. It was observed that the three samples delivered very close initial capacitances of 161, 166 and 166 F/g at 0.5 A/g, respectively, for LPC-0.3, LPC-0.4 and LPC-0.5 materials, which should be resulted from their similar SSAs [58]. Notably, with the increase of current density to 50 A/g, the LPC-0.5 still possessed a high capacitance retention of 82.5% as compared to LPC-0.3 (72.2% retention) and LPC-0.4 (77.1% retention) samples, further demonstrating the excellent rate capability of the LPC-0.5 sample. Even at a high mass loading of 8 mg/cm^2, the specific capacitance for LPC-0.5 still remained 146.1 F/g at 0.5 A/g and 102.2 F/g at 50 A/g (70% retention), which successfully indicated the practicability of LPC materials herein (Fig. S8 in Supporting information).

The electrochemical impedance spectroscopy (EIS) spectra of LPC-X (X = 0.3, 0.4 and 0.5) were also measured and fitted by equivalent circuit model (Fig. 3f). Obviously, impedance spectra were mainly consisted of three regions: the semicircles at high-frequency region, the 45° slope lines at mid-frequency, and vertical lines in low-frequency. The nearly vertical low-frequency lines represented the ideal capacitive behaviors. At mid-frequency region, the negligible 45° slope lines assigned to Warburg resistance ef-

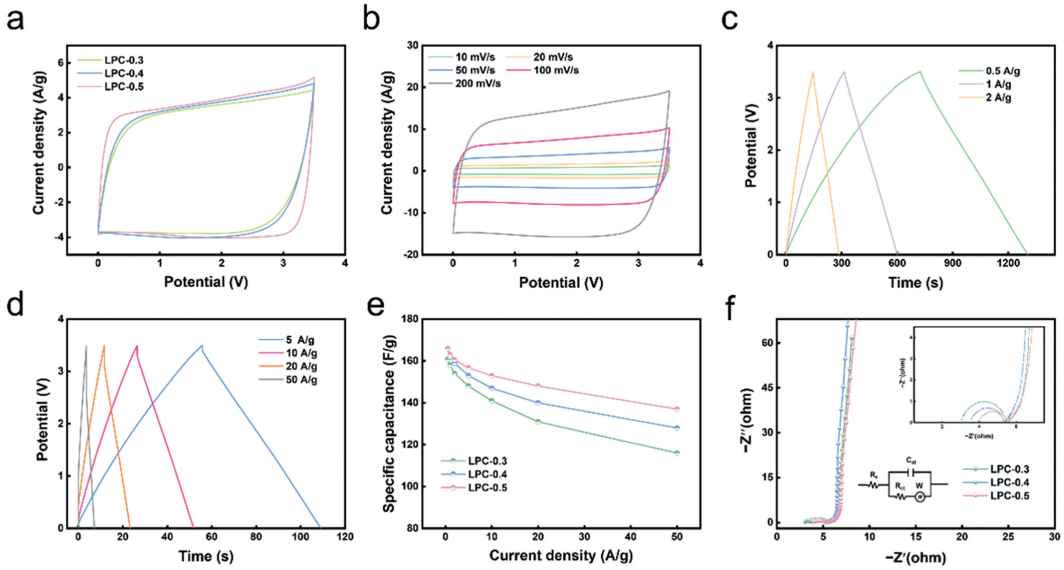

Fig. 3. The electrochemical properties of LPC-X (X = 0.3, 0.4 and 0.5) materials in $EMIBF_4$ ILs. (a) CV curves of LPC-Xs measured at 50 mV/s. (b) CV curves of LPC-0.5 under different scan rates ranged from 10 mV/s to 200 mV/s. (c, d) GCD curves of LPC-0.5 tested from 0.5 A/g to 50 A/g. (e) The rate capabilities. (f) EIS spectra. The inset exhibited the equivalent circuit model of EIS.

ficiently reflected the fast ion diffusion capability within LPC-Xs electrodes. The distance of the semicircles at the high-frequency, designated the charge transfer resistance (R_{ct}), which was obtained to be 2.42, 1.84 and 1.59 Ω for LPC-0.3, LPC-0.4, and LPC-0.5, respectively. Such small R_{ct} can be attributed to the 3D interconnected porous architecture, high electrical conductivity and appropriate content of dopants, synergistically providing accessible pathways for ion diffusion and electron charge. In addition, the intercept on the real axis at high frequency corresponded to the equivalent series resistance (R_S), which represented the intrinsic resistance of electrode materials, the ionic resistance of electrolyte, and the contact resistance between the electrode and current collector. It can be noticeable that the LPC-0.5 exhibited a slightly higher R_S value than those for LPC-0.3 and LPC-0.4, which can be attributed from the well-developed porous structure restricting the continuous channels of electron diffusion to a certain degree. Nevertheless, the LPC-0.3 and LPC-0.4 exhibits higher O/N heteroatom concentration relative to LPC-0.5, which aggravated the decomposition of electrolyte components, thereby resulting in lower capacitance performances during the high-voltage application [59]. Such observations were in good accordance with the CV and GCD analyses above, collectively confirming the good kinetics and excellent rate capability of LPC-X (X = 0.3, 0.4 and 0.5) electrodes.

Energy density, power density, as well as the cycling stability are other indicators to probe the practicability of electrode materials in supercapacitors. In this case, symmetrical supercapacitor devices based on the optimal LPC-0.5 (LPC-0.5//LPC-0.5) were assembled as illustrated in Fig. 4a. The Ragone plot qualitatively depicted the relationship between energy density and power density (Fig. 4b), which presented an approximately parallel line to the *x*-axis with the increased power density, implying its excellent energy-power rating. Furthermore, a maximum energy density of 72 Wh/kg can be reached at the power density of 320 W/kg, and still maintained the high value of 59 Wh/kg even at an ultra-high power density of 59 kW/kg, which was superior to most of the previous reported lignin derived porous carbon in symmetrical supercapacitors with ionic liquid electrolyte (Table S3 in Supporting information). In addition, it was found in Fig. 4c that the LPC-0.5 sustained an impressive cycling stability with capacitance retention of 93.1% after 10,000 cycles at 2 A/g. The satisfactory coulombic efficiency of about 98% was obtained and further confirmed the high electrochemical reversibility of the LPC-0.5 electrode. All these results strongly indicated that the LPC-X materials, especially LPC-0.5, can be rendered as high performance promising electrodes for supercapacitors with $EMIBF_4$ IL electrolytes.

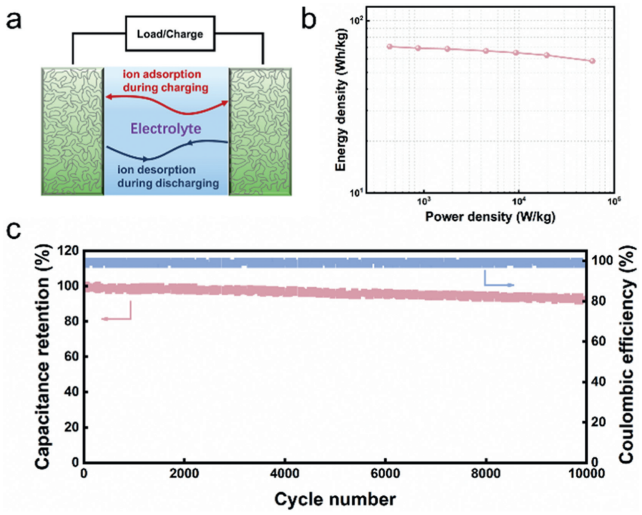

Fig. 4. (a) Schematic diagram of the assembled supercapacitor device with IL electrolyte. (b) The Ragone plot of LPC-0.5 material. (c) Stability testing conducted at 2 A/g for 10 000 cycles of LPC-0.5 material.

In summary, lignin-derived porous carbon with rich mesoporisity were designed *via* a facile template strategy, and validated as efficacious electrode for supercapacitors with IL electrolytes. The as-prepared samples not only exhibited 3D interconnected hierarchical porous scaffold with accessible mesopore, large SSA and favorable pore size distribution, but held high graphitization degree as well as low heteroatom content, cooperatively facilitating the ion and electron kinetics and thus superior electrochemical performance. Benefited from these advantages, the optimal LPC-0.5 sample delivered a high specific capacitance of 166 F/g at the current density of 0.5 A/g with superior rate capability (capacitance re-

tention of 82.5% at 50 A/g) in $EMIBF_4$ electrolyte. Particularly, the symmetric capacitor also reached a high integrated energy-power density of 59 Wh/kg at 59 kW/kg together with excellent cycle stability (93.1% capacitance retention after 10,000 cycles at 2 A/g). This work provided new insights into designing porous carbon materials from lignin-based raw materials for high-performance supercapacitors with IL electrolytes.

Declaration of competing interest

The authors declare that they have no known competing financial interests or personal relationships that could have appeared to influence the work reported in this paper.

Acknowledgments

This work was supported by the National Natural Science Foundation of China (No. 22209014), Beijing Forestry University Outstanding Young Talent Cultivation Project (No. 2019JQ03017), National Science Fund for Distinguished Young Scholars (No. 32225034), and China-111 Project (No. BP0820033).

Supplementary materials

Supplementary material associated with this article can be found, in the online version, at doi:10.1016/j.cclet.2023.108187.

References

[1] P. Simon, Y. Gogotsi, Nat. Mater. 19 (2020) 1151–1163.
[2] J. Liu, H. Yuan, X. Tao, et al., EcoMat 2 (2020) e12019.
[3] H. Yuan, L. Kong, T. Li, et al., Chin. Chem. Lett. 28 (2017) 2180–2194.
[4] Z. Song, L. Miao, H. Duan, et al., Angew. Chem. Int. Ed. 61 (2022) e202208821.
[5] Z. Song, L. Miao, L. Ruhlmann, et al., Adv. Funct. Mater. 22 (2022) 2208049.
[6] W. Raza, F. Ali, N. Raza, et al., Nano Energy 52 (2018) 441–473.
[7] Poonam, K. Sharma, A. Arora, et al., J. Energy Storage 21 (2019) 801–825.
[8] S. Kumar, G. Saeed, L. Zhu, et al., Chem. Eng. J. 403 (2021) 126352.
[9] L. Miao, Y. Lv, D. Zhu, et al., Chin. Chem. Lett. (2022) 107784.
[10] Z. Ling, Z. Wang, M. Zhang, et al., Adv. Funct. Mater. 26 (2016) 111–119.
[11] Z. Li, S. Gadipelli, H. Li, et al., Nat. Energy 5 (2020) 160–168.
[12] Q. Chen, J. Jin, M. Song, et al., Adv. Mater. 34 (2022) 2107992.
[13] K.L. Van Aken, M. Beidaghi, Y. Gogotsi, Angew. Chem. Int. Ed. 54 (2015) 4806–4809.
[14] J. Wu, Chem. Rev. 122 (2022) 10821–10859.
[15] T.S. Bhat, P.S. Patil, R.B. Rakhi, J. Energy Storage 50 (2022) 104222.
[16] P.H.L. Ferreira, A.M. Sampaio, L.J.A. Siqueira, Electrochim. Acta 410 (2022) 139982.
[17] A. Eftekhari, Energy Storage Mater. 9 (2017) 47–69.
[18] L. Miao, Z. Song, D. Zhu, et al., Energy Fuels 35 (2021) 8443–8455.
[19] L. Feng, K. Wang, X. Zhang, et al., Adv. Funct. Mater. 28 (2018) 1704463.
[20] M. Xu, Y. Liu, Q. Yu, et al., Chin. Chem. Lett. 32 (2021) 184–189.
[21] P.F.R. Ortega, G.A. de Santos, J.P.C. Trigueiro, et al., J. Phys. Chem. C 124 (2020) 15818–15830.
[22] S. Yuan, Q. Gao, C. Ke, et al., ChemElectroChem 9 (2022) e202101182.
[23] G. Wang, L. Zhang, J. Zhang, Chem. Soc. Rev. 41 (2012) 797–828.
[24] Y. Qin, L. Miao, M. Mansuer, et al., ACS Appl. Mater. Interfaces (2022) 33328–33339.
[25] J. Liu, L. Ma, Y. Zhao, et al., Chem. Eng. J. 411 (2021) 128573.
[26] N. Yang, L. Ji, H. Fu, et al., Chin. Chem. Lett. 33 (2022) 3961–3967.
[27] K.A. Owusu, Z. Wang, L. Qu, et al., Chin. Chem. Lett. 31 (2020) 1620–1624.
[28] X. Zheng, L. Miao, Z. Song, et al., J. Mater. Chem. A 10 (2022) 611–621.
[29] B. Wang, T. Ruan, Y. Chen, et al., Energy Storage Mater. 24 (2020) 22–51.
[30] K.S. Kumar, N. Choudhary, Y. Jung, et al., ACS Energy Lett. 3 (2018) 482–495.
[31] L. Zhang, P. Cai, Z. Wei, et al., J. Colloid Interf. Sci. 588 (2021) 637–645.
[32] J. Guo, Y. Yu, L. Sun, et al., Chem. Eng. J. 397 (2020) 125517.
[33] M. Ramu, J.R. Chellan, N. Goli, et al., Adv. Funct. Mater. 30 (2020) 1906586.
[34] J. Du, A. Chen, X. Gao, et al., ACS Appl. Mater. Interfaces 14 (2022) 11750–11757.
[35] S. Park, J. Kim, K. Kwon, Chem. Eng. J. 446 (2022) 137116.
[36] Z. Bi, Q. Kong, Y. Cao, et al., J. Mater. Chem. A 7 (2019) 16028–16045.
[37] D.V. Chernysheva, Y.A. Chus, V.A. Klushin, et al., ChemSusChem 11 (2018) 3599–3608.
[38] S. Zhao, X. Kang, H. Fan, et al., Micropor. Mesopor. Mat. 329 (2022) 111518.
[39] K. Chen, S. Weng, J. Lu, et al., Micropor. Mesopor. Mat. 320 (2021) 111106.
[40] L. Mo, S. Jia, S. Lin, et al., Int. J. Energ. Res. 46 (2021) 2373–2384.
[41] Z. Peng, C. Wang, Z. Zhang, et al., Adv Mater Interfaces 6 (2019) 1901393.
[42] W. Li, G. Wang, W. Sui, et al., Carbon 196 (2022) 819–827.
[43] Y. Fu, Y. Qian, A. Zhang, et al., ACS Sustain. Chem. Eng. 10 (2022) 5421–5429.
[44] C. Liu, Y. Hou, Y. Li, et al., J. Colloid Interf. Sci. 614 (2022) 566–573.
[45] F. Shi, Y. Tong, H. Li, et al., J. Energy Storage 52 (2022) 104992.
[46] R. Zhong, H. Zhang, Y. Zhang, et al., J. Energy Storage 51 (2022) 104346.
[47] F. Wang, L. Chen, H. Li, et al., Chin. Chem. Lett. 31 (2020) 1986–1990.
[48] J. Yan, L. Miao, H. Duan, et al., Chin. Chem. Lett. 33 (2022) 2681–2686.
[49] J. Yin, W. Zhang, N.A. Alhebshi, et al., Small Methods 4 (2020) 1900853.
[50] Y. Li, Y. Chen, X. He, et al., Chem. Eng. J. 431 (2022) 133907.
[51] G. Ping, L. Miao, A. Awati, et al., Chin. Chem. Lett. 32 (2021) 3811–3816.
[52] J. Wang, Y. Qian, L. Li, et al., ChemSusChem 13 (2020) 4420–4427.
[53] B. Zhang, D. Yang, Y. Qian, et al., Ind. Crop. Prod. 155 (2020) 112773.
[54] S. Chatterjee, T. Saito, ChemSusChem 8 (2015) 3941–3958.
[55] Z. Song, H. Duan, L. Miao, et al., Carbon 168 (2020) 499–507.
[56] Z. Song, L. Miao, L. Li, et al., Carbon 180 (2021) 135–145.
[57] K. Liu, C. Yu, Y. Xie, et al., J. Energy Chem. 72 (2022) 291–298.
[58] J. Li, N. Wang, J. Tian, et al., Adv. Funct. Mater. 28 (2018) 1806153.
[59] C.F. Liu, Y.C. Liu, T.Y. Yi, et al., Carbon 145 (2019) 529–548.